



ACM: 30090 Mathematical Biology

The Influence of Synaptic Plasticity on Critical Coupling Estimates for Neural Populations

Author:

David Kelly

Paper Authors:

Kaitlyn Toth & Dan Wilson

Abstract

We investigate how spike-timing-dependent plasticity (STDP) and higher-order synaptic filtering influence the emergence and stability of synchrony in networks of conductance-based neurons. Building on the phase-reduction framework of Toth & Wilson (2024), we first implement a population of Rubin-Terman thalamic neurons with static synapses and with plastic (soft-bound Hebbian) synapses—reproducing the key synchronisation phenomena reported by Toth and Wilson. We then introduce a second-order synaptic coupling model—capturing both rise and decay dynamics of postsynaptic conductances—and compare its effects to classical first-order coupling. In homogeneous and heterogeneous excitatory networks, STDP robustly promotes phase cohesion—even as neurons achieve full synchrony they continue to undergo firing-order switches—whereas in inhibitory networks it destabilises synchrony. Second-order coupling, by contrast, suppresses coherence in both excitatory and inhibitory regimes.

Contents

1	Introduction	1
2	Methods	3
2.1	Overview of the Model	3
2.2	Modelling Synaptic Plasticity	4
2.3	Phase Reduction	4
2.4	Computational Simulation	5
2.5	Extension: Second-Order Synaptic Coupling	5
3	Numerical Analysis	7
3.1	Homogeneous Networks	7
3.1.1	Inhibitory Networks	7
3.1.2	Excitatory Networks	8
3.2	Heterogeneous Networks	9
3.2.1	Inhibitory Networks	9
3.2.2	Excitatory Networks	10
3.3	Extension: Second-Order Coupling	11
3.3.1	Inhibitory Networks	11
3.3.2	Excitatory Networks	12
3.4	Phase Dynamics and Firing Order	13
4	Conclusion and Discussion	15
References		17
A	Code Availability	18
B	Detailed Neural Model Equations	18

1 Introduction

Neurons communicate with one another using electrical signals known as *action potentials* or “spikes”. These spikes travel along the axon of a neuron and are transmitted across *synapses*—specialised junctions between neurons—via chemical neurotransmitters. When one neuron spikes, it can either excite or inhibit the next neuron in the network, depending on the type of neurotransmitter and receptor involved. This system of excitation and inhibition forms the basis of all brain activity, from muscle movement to perception, memory, and emotion.

The strength of these synaptic connections, known as synaptic weight or efficacy, is not fixed. Instead, it can change over time in response to the activity of the neurons involved. This process is called *synaptic plasticity*, and it is one of the most fundamental biological mechanisms underlying learning and memory. The brain can rewire itself by strengthening or weakening synapses based on experience. One of the most well-studied forms of plasticity is *spike-timing dependent plasticity* (STDP), in which the precise timing of spikes determines whether a synapse becomes stronger or weaker [1].

In STDP, if a presynaptic neuron fires just before a postsynaptic neuron, the synapse is typically strengthened—a process known as long-term potentiation (LTP). Conversely, if the postsynaptic neuron fires first, the synapse is often weakened—called long-term depression (LTD). This timing-based rule is supported by a large body of experimental work and is thought to underlie the brain’s ability to detect causality and store temporal information [3]. Over time, STDP reshapes the network structure, modifying how strongly neurons are coupled.

The brain often relies on *neural synchronisation*—the tendency of neurons to fire in a coordinated fashion—to support cognitive functions. Oscillatory synchronisation has been observed in attention, memory encoding, and sensory integration, and is thought to enhance communication between brain regions [2]. However, abnormal synchrony can also contribute to disease. In Parkinson’s disease, for instance, excessive synchronisation in certain brain areas is associated with motor impairment [6].

To investigate the emergence and stability of synchronisation, researchers frequently use mathematical models of neural dynamics. One common class of models are conductance-based neurons, which describe how ion channels regulate voltage changes across the membrane. These models can be simplified using phase reduction techniques, which reduce the dynamics of each neuron to a single variable representing its phase in an oscillatory cycle. This allows researchers to focus on interactions between neurons without simulating every ionic detail [4].

In the paper by Toth and Wilson (2024), the authors investigate how STDP impacts

the minimum synaptic strength—called the *critical coupling strength*—required to maintain phase cohesion in a population of coupled neurons. *Phase cohesion* refers to the condition where neurons’ phases stay within a bounded range rather than drifting apart. In networks with static synapses, synchrony depends only on the coupling strength and network structure. But in adaptive networks with STDP, the relative timing of spikes—especially changes in firing order—can significantly influence the outcome.

Toth and Wilson demonstrate that when spike order frequently switches, the synchronising effect of coupling is weakened. In contrast, consistent ordering can allow STDP to stabilise synchrony even in networks of excitatory neurons, which usually desynchronise under static coupling. Their results highlight the dynamic relationship between plasticity and synchronisation, providing new insight into how real neural networks might maintain coherent activity over time.

In this project, I will recreate the exact thalamic neuron model used by Toth & Wilson (2024), implement both static synapses and Hebbian spike-timing-dependent plasticity (STDP), and monitor network behaviour with the Kuramoto order parameter to quantify phase coherence and synchrony. I will also investigate the changes in spike ordering (ordinal switches) in an excitatory network with STDP. To extend this work, I introduce a third approach to modelling synapses by incorporating *second-order synaptic coupling*, which considers not only direct interactions but also interactions modulated by the past activity of connected neurons. Unlike the original study, which focused solely on first-order coupling, this extension aims to explore how memory-like effects in synaptic interactions influence network dynamics. I will compare synchronisation behaviour under this model in both excitatory and inhibitory populations to examine whether second-order mechanisms can enhance or suppress synchrony.

2 Methods

2.1 Overview of the Model

The model used by Toth and Wilson simulates a population of N conductance-based neurons that are synaptically coupled. Each neuron follows a modified Rubin–Terman model for thalamic neurons, which includes leak, sodium, potassium, and low-threshold calcium ionic currents. The voltage dynamics for neuron i are governed by the following system of differential equations:

$$\begin{aligned} C\dot{V}_i &= -I_L(V_i) - I_{Na}(V_i, h_i) - I_K(V_i, h_i) - I_T(V_i, r_i) + I_{\text{stim},i} - \frac{1}{N-1} \sum_{j \neq i} I_{\text{syn}}^{j \rightarrow i}(s_j, V_i), \\ \dot{h}_i &= \frac{h_\infty - h_i}{\tau_h}, \\ \dot{r}_i &= \frac{r_\infty - r_i}{\tau_r}, \\ \dot{s}_i &= \frac{c_1(1 - s_i)}{1 + \exp(-(V_i - V_T)/\sigma_T)} - c_2 s_i. \end{aligned} \tag{2.1}$$

Here, V_i represents the membrane voltage of neuron i , h_i and r_i are gating variables for sodium and calcium currents, respectively, and s_i is a synaptic gating variable. The ionic currents include the leak (I_L), sodium (I_{Na}), potassium (I_K), and low-threshold calcium (I_T) terms.

The external stimulus current $I_{\text{stim},i}$ governs whether the population is homogeneous or heterogeneous. In *homogeneous simulations*, this value is fixed across all neurons as $I_{\text{stim},i} = 5$. In *heterogeneous configurations*, $I_{\text{stim},i}$ is drawn independently from a uniform distribution over the interval [4.84, 5.16] to induce diversity in firing frequencies.

Synaptic coupling is mediated by the synaptic current from neuron j to neuron i , given by:

$$I_{\text{syn}}^{j \rightarrow i} = K g_{j \rightarrow i}(t) s_j(t)(V_i - E_{\text{syn}}), \tag{2.2}$$

where K is the maximum synaptic conductance, $g_{j \rightarrow i}(t)$ is the plastic synaptic weight subject to STDP, $s_j(t)$ is the synaptic gating variable, and E_{syn} is the synaptic reversal potential.

The sign of E_{syn} determines whether the coupling is excitatory or inhibitory. It is taken to be -80 mV in inhibitory simulations and 0 mV in excitatory simulations, because setting $E_{\text{syn}} = -80$ mV (near the chloride reversal potential) produces hyperpolarising (inhibitory) currents, whereas choosing $E_{\text{syn}} = 0$ mV (the non-specific cation reversal potential) yields

depolarising (excitatory) currents.

2.2 Modelling Synaptic Plasticity

Synaptic weights evolve dynamically according to a soft-bounded Hebbian spike-timing dependent plasticity (STDP) rule. Each synaptic weight $g_{j \rightarrow i}(t)$ is updated whenever either the presynaptic neuron j or the postsynaptic neuron i spikes. Spikes are detected when the membrane voltage crosses -30 mV with positive slope. The STDP rule is defined by:

$$g_{\alpha \rightarrow \beta}(t_i^+) = \begin{cases} g_{\alpha \rightarrow \beta}(t_i^-) + A_+(1 - g_{\alpha \rightarrow \beta}(t_i^-))e^{-\Delta t_{\alpha \rightarrow \beta}/\tau_+}, & 0 < \Delta t_{\alpha \rightarrow \beta} < t_c, \\ g_{\alpha \rightarrow \beta}(t_i^-) - A_-(g_{\alpha \rightarrow \beta}(t_i^-) - g_{\min})e^{\Delta t_{\alpha \rightarrow \beta}/\tau_-}, & -t_c < \Delta t_{\alpha \rightarrow \beta} \leq 0, \\ g_{\alpha \rightarrow \beta}(t_i^-), & |\Delta t_{\alpha \rightarrow \beta}| \geq t_c, \end{cases} \quad (2.3)$$

where $\Delta t_{\alpha \rightarrow \beta} = t_\beta - t_\alpha$ is the time difference between postsynaptic and presynaptic spikes, A_+ and A_- are learning rates, τ_+ and τ_- are the time constants for potentiation and depression, and g_{\min} is the lower bound for the synaptic weight. Updates occur only if the spike time difference falls within the time window $|\Delta t_{\alpha \rightarrow \beta}| < t_c$.

2.3 Phase Reduction

To analytically examine synchronisation, the conductance-based model is reduced to a phase description under the assumption of weak coupling. The phase θ_i of each neuron evolves as:

$$\dot{\theta}_i = \omega_i - \frac{\varepsilon K}{N-1} \sum_{j \neq i} Z_i(\theta_i) g_{j \rightarrow i}(t) s_j(t) (V_i - E_{\text{syn}}), \quad (2.4)$$

where $Z_i(\theta)$ is the *infinitesimal phase response curve (PRC)* for neuron i , quantifying its sensitivity to external input at different phases. The PRC is computed numerically using the adjoint method. This phase model allows analytical derivation of an upper bound on the *critical coupling strength* K_{crit} necessary to maintain *phase cohesion*, i.e., bounded phase differences between neurons within a specified arc length ν .

To quantify network synchrony, we use the *Kuramoto order parameter*:

$$\zeta(t) = \left| \frac{1}{N} \sum_{i=1}^N e^{i\theta_i(t)} \right|, \quad (2.5)$$

where $\zeta = 1$ indicates perfect synchrony and values near 0 correspond to desynchronisation. Since the phase is not directly measurable from the conductance-based simulations, spike

times are used to infer phase trajectories via linear interpolation between successive spikes. This metric is used to track the degree of phase alignment across the network throughout all simulations.

2.4 Computational Simulation

Numerical simulations were conducted to validate analytical predictions. The full conductance-based model was implemented in Python and integrated using a forward–Euler method with a fixed time step of 0.001 ms. For each network size (e.g., $N = 5$), both excitatory and inhibitory coupling scenarios were simulated, with and without STDP.

We examined two coupling regimes: *static synapses*, in which the synaptic weights $g_{j \rightarrow i}$ remain fixed at 1 throughout the simulation, and *plastic synapses*, which evolve over time under the STDP rule described above. Each configuration (static vs. plastic, excitatory vs. inhibitory) was simulated and compared against the theoretical upper bound on critical coupling strength.

All simulation parameters—including ionic and synaptic parameters—match exactly those reported in the original study by Toth and Wilson (2024) to ensure direct comparability.

2.5 Extension: Second-Order Synaptic Coupling

To extend the work of Toth and Wilson, we introduce a refined model of synaptic transmission based on *second-order synaptic filtering*, which more accurately captures the temporal dynamics of postsynaptic activation. Rather than defining the synaptic variable s_j through a first-order decay process as in the original model, we define it via a second-order differential equation:

$$\left(1 + \tau_s \frac{d}{dt}\right)^2 s_j = p_0 \sum_{t_j^q < t} \delta(t - t_j^q), \quad (2.6)$$

where τ_s is the synaptic time constant and p_0 controls the magnitude of synaptic activation in response to a presynaptic spike. The right-hand side consists of a sum over Dirac delta functions, each corresponding to a presynaptic spike from neuron j occurring at time t_j^q . This formulation describes the postsynaptic current as a second-order low-pass filter of the presynaptic spike train, yielding smoother and more biologically plausible temporal responses than the standard exponential decay.

For numerical integration, Eq. (2.6) is reformulated as a system of two coupled first-order

differential equations:

$$\begin{cases} \frac{ds_j}{dt} = -\frac{s_j}{\tau_s} + \frac{p_j}{\tau_s}, \\ \frac{dp_j}{dt} = -\frac{p_j}{\tau_s} + \frac{p_0}{\tau_s} \sum_{t_j^q < t} \delta(t - t_j^q), \end{cases} \quad (2.7)$$

where $p_j(t)$ is an auxiliary variable that tracks the impulse response buildup due to presynaptic spikes. Each time neuron j fires, the delta function introduces a discontinuous jump of magnitude p_0 into $p_j(t)$, which in turn drives the dynamics of the synaptic variable $s_j(t)$.

In this extension, we focus solely on the effect of second-order dynamics and do not incorporate STDP. That is, the synaptic weight matrix $g_{j \rightarrow i}$ is now taken to be fixed and uniform for all neuron pairs. Specifically, we assume an all-to-all coupling architecture where $g_{j \rightarrow i} = 0.1$ for all i, j . Thus, plasticity is effectively replaced by temporally enriched synaptic filtering, allowing us to isolate the role of synaptic memory in shaping network synchronisation.

This second-order formulation offers two key advantages. First, it enables sharper temporal control over synaptic activation, as both the rise and decay phases are modulated by τ_s . Second, it allows a more realistic approximation of postsynaptic conductance transients, particularly in models where rapid summation of inputs or dendritic processing plays a role.

The dynamics resulting from this second-order model are illustrated in Fig. 1, which shows the time course of $s(t)$ following a single presynaptic spike when $\tau_s = 1$ and $p_0 = 1$. In this case, the peak occurs at $t = \tau_s$, and the shape of the response reflects the symmetric rise and decay characteristic of a critically damped second-order system.

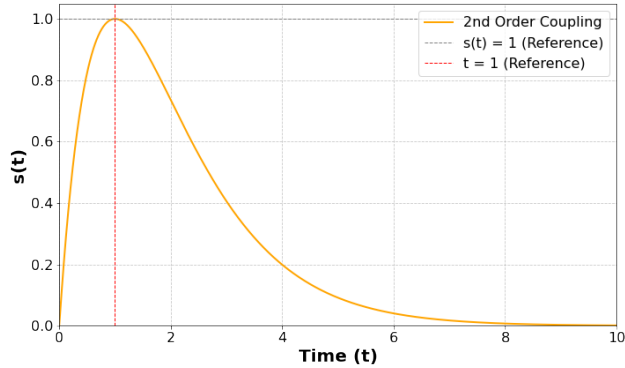


Figure 1: Second order coupling with $\tau_s = 1$ and $p_0 = 1$. This causes $s(t)$ to have a peak response of 1 at $t = 1$.

3 Numerical Analysis

3.1 Homogeneous Networks

We investigate the effect of spike-timing-dependent plasticity (STDP) on the synchronisation behaviour of homogeneous neural populations by simulating networks of conductance-based neurons. Both inhibitory and excitatory coupling scenarios are analysed using voltage traces and the Kuramoto order parameter $\zeta(t)$, which quantifies phase coherence.

3.1.1 Inhibitory Networks

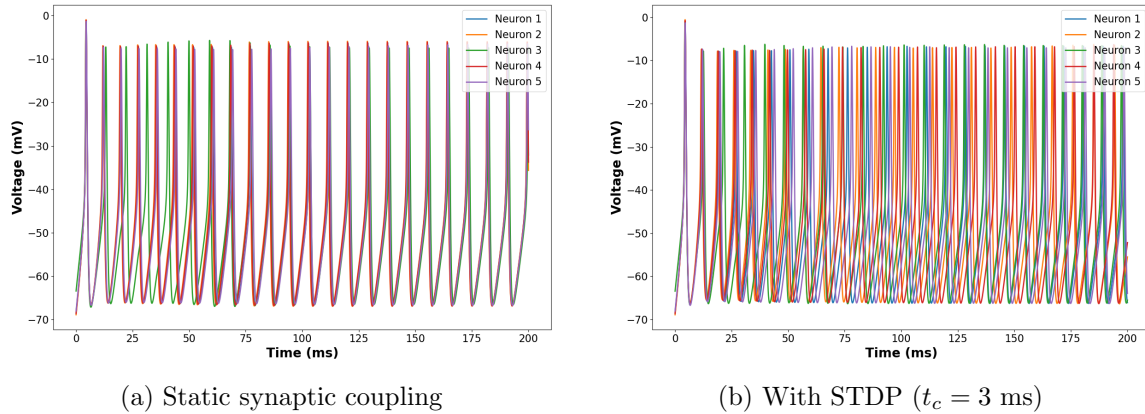


Figure 2: Membrane potentials of each neuron in an inhibitory network ($N = 5$), simulated with (a) fixed synapses and (b) spike-timing-dependent plasticity.

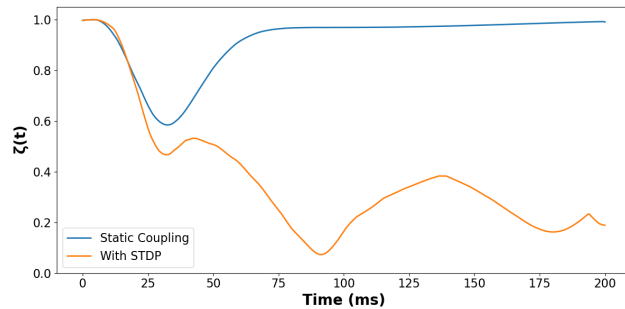


Figure 3: Kuramoto order parameter $\zeta(t)$ for the same inhibitory networks. Static coupling (blue) remains near coherence, whereas STDP (orange) drives the system toward desynchronisation.

Figure 2 shows the membrane potentials of $N = 5$ inhibitory neurons. In the case of static synaptic coupling (panel a), neurons become synchronised after a short period of time with overlapping voltage traces. When STDP is introduced (panel b), this synchrony is lost, and the population becomes desynchronised.

In the static-synapse case, due to synchronisation, we can estimate the network oscillation frequency by counting peaks in the voltage trace. For example, between $t = 75$ ms

and $t = 150$ ms, we observe 9 peaks over $\Delta t = 150 - 75 = 75$ ms = 0.075 s. Hence,

$$f \approx \frac{9}{75 \text{ ms}} = \frac{9}{0.075 \text{ s}} \approx 120 \text{ Hz}.$$

This lies at the upper end of the “high-gamma” band (20–120 Hz), oscillations that have been implicated in feature binding and visual processing in cortex [5].

This behaviour is quantified in Fig. 3, where the Kuramoto order parameter $\zeta(t)$ remains high under static coupling (blue curve), indicating strong phase alignment. However, in the presence of STDP (orange curve), $\zeta(t)$ decays over time, reflecting a transition to desynchronisation.

3.1.2 Excitatory Networks

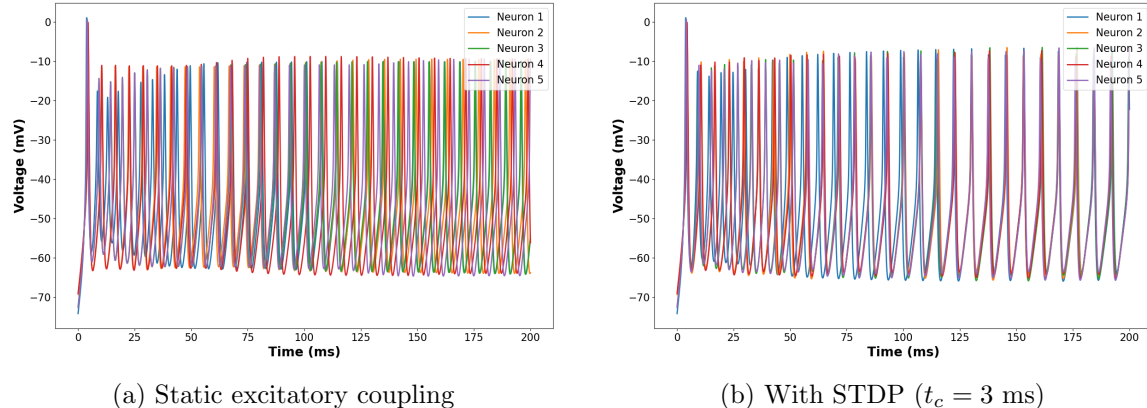


Figure 4: Voltage traces for each neuron in an excitatory network ($N = 5$), simulated with (a) fixed synapses and (b) spike-timing-dependent plasticity.

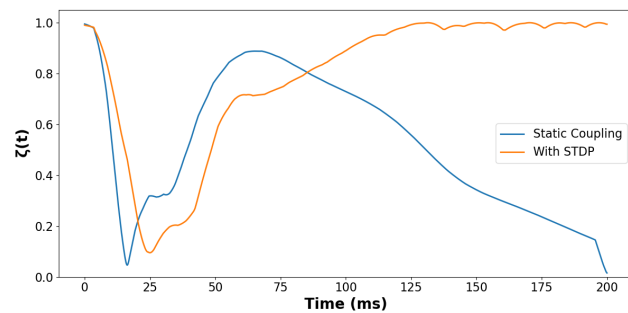


Figure 5: Kuramoto order parameter $\zeta(t)$ for the excitatory network. Static coupling (blue) settles to partial synchronisation, while STDP (orange) drives the population toward full synchrony.

Figure 4 presents results for excitatory networks. With static coupling (panel a), neurons display some regularity, but full synchrony is not achieved. When STDP is enabled (panel b), voltage traces align increasingly well, showing that plasticity reinforces synchronisation. This differs from inhibitory systems where STDP prevents synchrony. The frequency of

these coherent oscillations is notably higher than that observed with static coupling in the inhibitory case, reaching approximately 140 Hz using the same analysis method described above.

As illustrated in Fig. 5, the Kuramoto order parameter for static coupling (blue) fluctuates from high to low indicating varying levels of synchrony over time. As time progresses this system appears to become completely asynchronous. In contrast, the STDP case (orange) steadily approaches $\zeta = 1$, indicating full synchronisation across the population.

3.2 Heterogeneous Networks

To explore how synaptic plasticity influences more biologically realistic networks, we extend our analysis to heterogeneous populations by drawing the external stimulus current $I_{\text{stim},i}$ for each neuron from a uniform distribution. This introduces variability in the intrinsic firing frequencies, creating a richer and more complex dynamical landscape than the homogeneous setup.

3.2.1 Inhibitory Networks

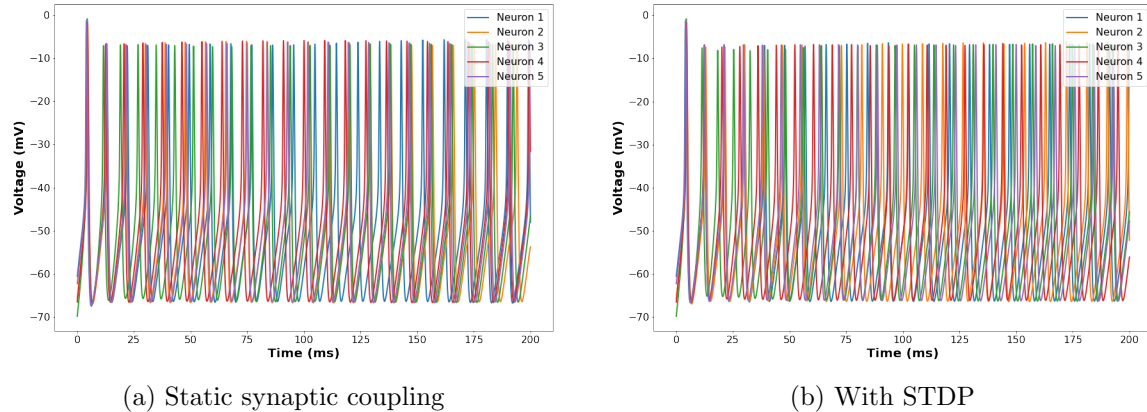


Figure 6: Voltage traces of heterogeneous inhibitory neurons with (a) static synapses and (b) STDP. Stimulus values are sampled from a uniform distribution.

As seen in Fig. 6, static coupling (a) preserves some synchrony despite heterogeneity, but with slightly offset spike timings. It does however exhibit markedly lower synchrony than that in Fig. 2 due to the now heterogeneous drive. When STDP is introduced (b), desynchronisation becomes more pronounced, mirroring the homogeneous case but with greater variability.

The Kuramoto order parameter in Fig. 7 confirms this. The static case maintains moderate coherence, whereas STDP leads to a steady decline in $\zeta(t)$, reflecting the destabilising

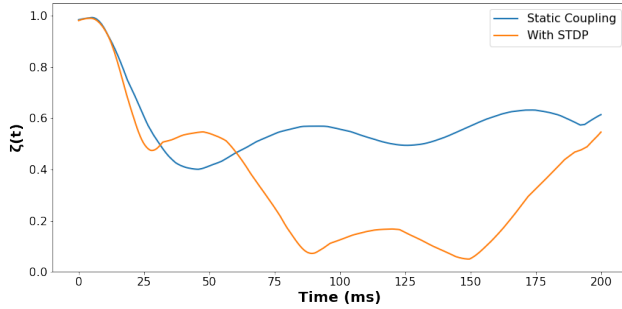


Figure 7: Kuramoto order parameter $\zeta(t)$ for heterogeneous inhibitory networks. Static coupling (blue) supports moderate synchrony, while STDP (orange) disrupts phase coherence over time.

influence of plasticity in inhibitory networks.

3.2.2 Excitatory Networks

In heterogeneous excitatory populations, Fig. 8 shows that static coupling alone (a) does not overcome the variability in spike timing. However, the introduction of STDP (b) gradually realigns firing, promoting convergence despite intrinsic differences.

This is quantitatively reflected in Fig. 9, where $\zeta(t)$ with STDP (orange) increases steadily toward unity, demonstrating robust phase locking even in the presence of heterogeneity. The static case (blue) stabilises at a lower value, indicating only partial synchrony.

Overall, heterogeneous simulations reinforce the findings from homogeneous networks. STDP undermines synchrony in inhibitory networks but enhances it in excitatory ones, even when neurons differ in their intrinsic drive. These results underline the robustness of plasticity-mediated synchronisation in excitatory populations and its sensitivity in inhibitory regimes.

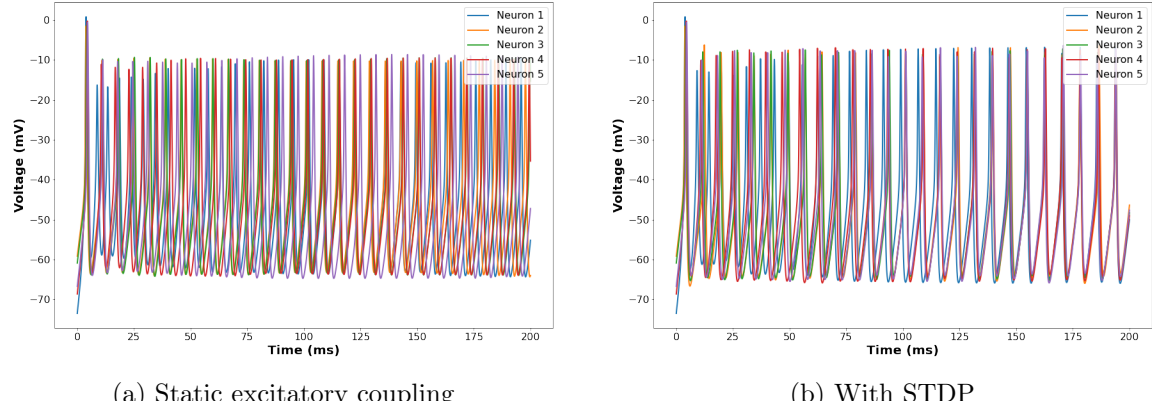


Figure 8: Membrane potentials in a heterogeneous excitatory network. With STDP (b), neurons progressively synchronise despite intrinsic differences.

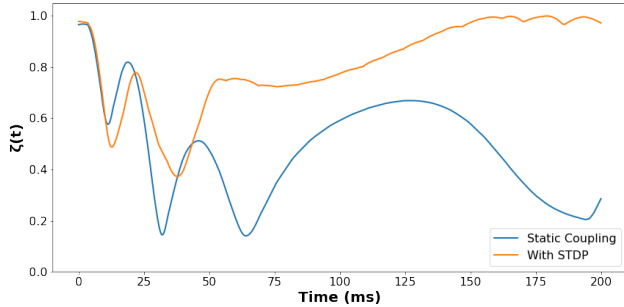


Figure 9: Kuramoto order parameter $\zeta(t)$ for the heterogeneous excitatory network. Static coupling (blue) yields limited synchrony. STDP (orange) enhances coherence and drives the population toward synchronisation.

3.3 Extension: Second-Order Coupling

To further explore how synaptic dynamics shape network synchronisation, we extend the work of Toth and Wilson by incorporating *second-order synaptic filtering*, as introduced in Section 2.5. This model captures more biologically realistic postsynaptic responses by allowing both rise and decay phases of synaptic conductance to evolve dynamically over time. Unlike the original first-order model, the second-order formulation introduces a memory-like effect that may either stabilise or destabilise phase alignment depending on the network configuration.

We analyse the behaviour of networks using this second-order model under both *homogeneous* and *heterogeneous* external drive, for both inhibitory and excitatory coupling. In each case, we evaluate voltage traces and track synchrony over time using the Kuramoto order parameter $\zeta(t)$.

3.3.1 Inhibitory Networks

In contrast to the case of static synaptic coupling under homogeneous drive—where neurons readily achieve and maintain synchrony—the introduction of second-order coupling disrupts this synchrony, preventing its sustained emergence (see Fig. 10). Under heterogeneous drive, both static and second-order coupling result in asynchronous network dynamics. This behaviour closely parallels that observed in networks with spike-timing dependent plasticity (STDP), where synchrony fails to develop regardless of whether the external drive is homogeneous or heterogeneous.

The Kuramoto order parameter plot (Fig. 11) illustrates that homogeneous drive maintains higher synchrony than heterogeneous after initial transients. This is expected, as homogeneous input reduces variability across the population, aligning spike timings and promoting coherence, whereas heterogeneous drive introduces desynchronising fluctuations that are exacerbated by the temporal filtering inherent in second-order synaptic dynamics.

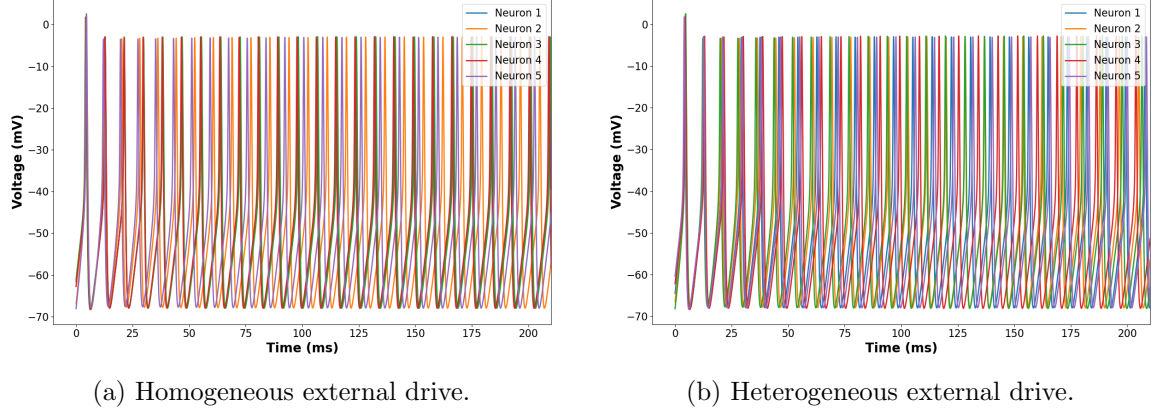


Figure 10: Voltage traces for inhibitory networks with second-order synaptic coupling. (a) Identical external stimulus across all neurons. (b) External stimuli drawn from a uniform distribution. Both cases show diminished synchrony relative to first-order models.

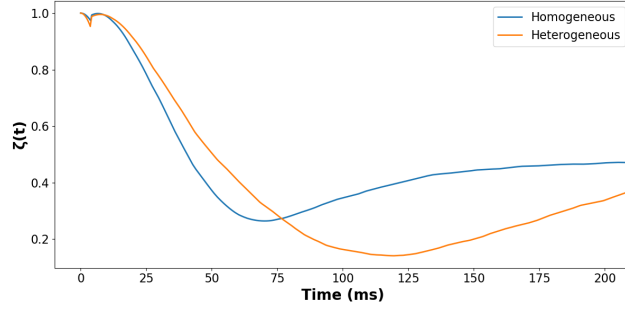


Figure 11: Kuramoto order parameter $\zeta(t)$ for inhibitory networks with second-order synaptic coupling. Homogeneous drive (blue) maintains higher phase coherence than heterogeneous input (orange), but both exhibit reduced synchrony over time.

3.3.2 Excitatory Networks

A similar pattern of dynamics is observed in excitatory networks with second-order coupling. In contrast to networks with STDP—where synchrony eventually emerges under both homogeneous and heterogeneous drive—second-order coupling prevents the development of synchrony in either case, even over extended time periods (see Fig. 12). The Kuramoto order parameter plot (Fig. 13) for the excitatory case mirrors that of the inhibitory network, with homogeneous drive sustaining higher levels of synchrony over time compared to the heterogeneous condition.

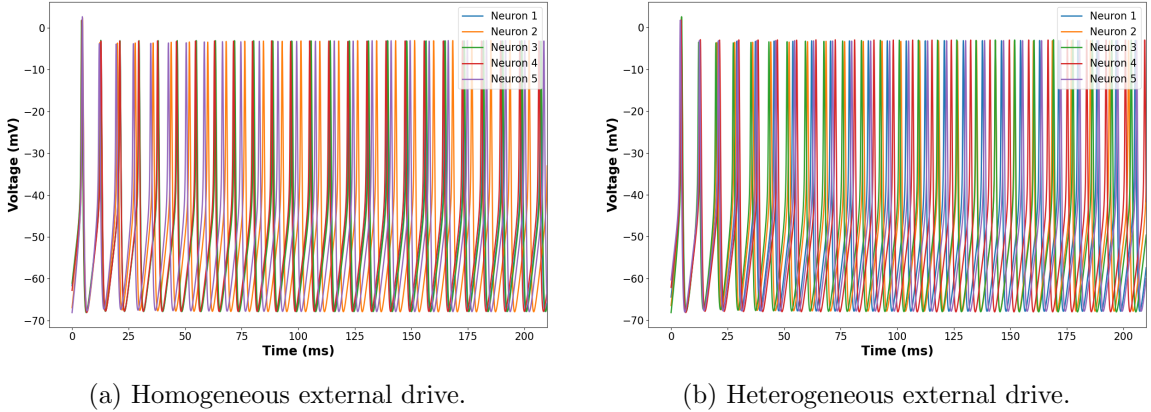


Figure 12: Voltage traces for excitatory networks with second-order synaptic coupling. (a) Identical external stimulus across all neurons (homogeneous). (b) External stimuli drawn from a uniform distribution (heterogeneous). Both cases show diminished synchrony relative to first-order models.

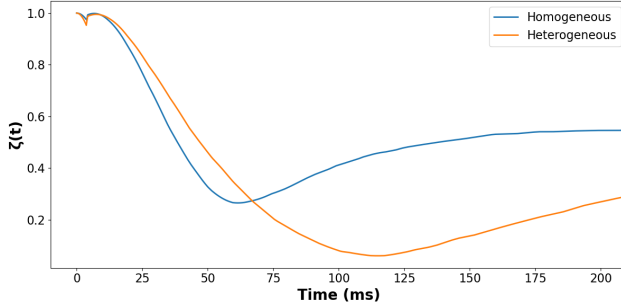


Figure 13: Kuramoto order parameter $\zeta(t)$ for excitatory networks with second-order synaptic coupling. Homogeneous drive (blue) maintains higher phase coherence than heterogeneous input (orange), but both exhibit reduced synchrony over time.

3.4 Phase Dynamics and Firing Order

To better understand how STDP influences firing relationships, Figs. 14 and 15 present voltage and phase deviation traces for two excitatory neural populations. In both figures, the top panels display the transmembrane voltage traces for each neuron, illustrating the high degree of synchrony across the network. The bottom panels show the quantity $\phi_i - \bar{\phi}$, where ϕ_i represents the phase of the i -th neuron and $\bar{\phi} = \frac{1}{N} \sum_{j=1}^N \phi_j$ is the average phase of the entire population. This deviation measures how far ahead or behind each neuron is in phase relative to the population mean.

Zero-crossings in the $\phi_i - \bar{\phi}$ traces indicate *ordinal firing-order switches*, where a neuron that was previously firing earlier than another now fires later, or vice versa. These crossings correspond precisely to the subtle lead-lag differences in spike timing visible in the voltage traces above, and they provide a quantitative way to track the dynamic reshuffling of firing order.

In Fig. 14, a homogeneous population of $N = 5$ neurons exhibits tightly synchronised

spiking, with phase deviations that remain small but occasionally cross zero—highlighting that STDP allows for dynamic flexibility in the order of firing, even under synchrony. Figure 15 extends this to a heterogeneous population with differing baseline inputs. Despite variability in individual drives, the network remains phase cohesive, with neurons continually reordering over time. Again, zero-crossings in the phase deviation curves mark firing-order transitions, underscoring the ability of STDP to support robust synchronisation while allowing for continual reorganisation in timing, even under heterogeneous input conditions.

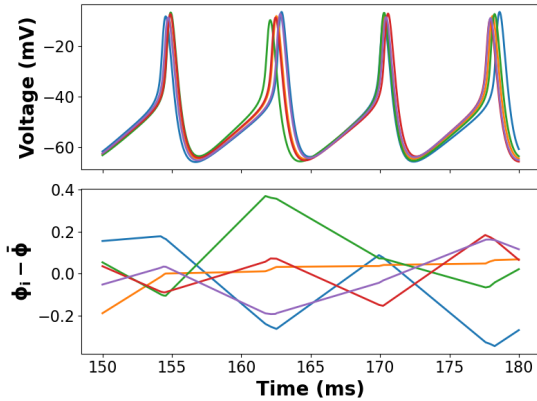


Figure 14: Voltage traces and phase deviations for $N = 5$ homogeneous, excitatory neurons under STDP. Ordinal firing-order switches in the full-order voltage traces correspond to zero-crossings in phase deviations.

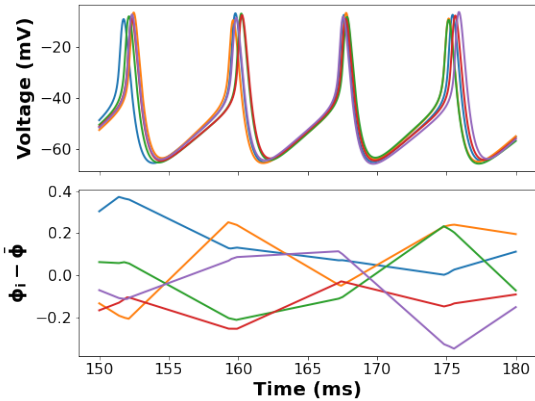


Figure 15: Voltage traces and phase deviations for $N = 5$ heterogeneous, excitatory neurons under STDP. Ordinal firing-order switches in the full-order voltage traces correspond to zero-crossings in phase deviations.

4 Conclusion and Discussion

Our simulations reveal that the simple choice of how synapses behave can make or break network rhythms. When every synapse had a fixed strength, inhibitory neurons locked into a neat, anti-phase rhythm as long as they all shared the same constant input. But the moment we introduced even slight variability in that drive—so each neuron received a different baseline current—their synchrony collapsed. Excitatory neurons, by contrast, never managed to pull together under static coupling, whether the drive was uniform or varied.

Introducing Hebbian STDP—where connections strengthen or weaken depending on which neuron fires first—turned both stories on their heads. Inhibitory networks that once synchronised under identical drive now fell apart as soon as their synapses began adapting to each spike’s timing; any fluctuation in firing order undermined their coherence. Excitatory networks, however, learned to fire in unison under plastic synapses, and they maintained that synchrony regardless of whether drives were homogeneous or heterogeneous. Notably, even though individual excitatory neurons continued to swap their positions in the firing sequence, those order switches never disrupted the overall phase alignment.

When we added a second-order filter to the synapses—so that postsynaptic currents rose and decayed smoothly rather than jumping instantaneously—the precise temporal information needed for phase locking was washed out. Both inhibitory and excitatory populations lost any coherent rhythm under this form of synaptic memory, emphasising that the shape of a synaptic response can be just as critical as its strength.

Despite these clear patterns, our work relies on several simplifying assumptions. We used a weak-coupling, phase-reduction approach appropriate only when synaptic inputs are small compared to each neuron’s intrinsic currents. Our neurons were modeled to fire tonically; bursting dynamics or networks with spike-frequency adaptation could follow very different rules. We implemented a single, soft-bound pair-based STDP rule, leaving open how triplet-based plasticity, homeostatic scaling, or heterosynaptic mechanisms might alter the balance of synchrony. Our framework was entirely deterministic, omitting the channel and synaptic noise present in real brains. Finally, all networks were small and fully connected, so phenomena arising in large, sparse, or modular architectures remain to be explored.

Moving forward, it will be important to relax the weak-coupling assumption—perhaps by developing higher-order phase models or direct numerical bifurcation analyses—to see how stronger synaptic inputs and larger voltage excursions influence synchrony. Incorporating alternative plasticity rules and homeostatic feedback will help us understand how different forms of learning cooperate or compete in shaping network rhythms. Adding

stochastic elements will test the robustness of our findings in noisy environments. Extending the framework to bursting neurons or adapting networks will reveal how slow currents interact with plasticity and filtering. And finally, scaling up to realistic connectivity patterns, complete with delays and adaptive rewiring, will bridge the gap between our idealised models and the complex synchrony observed *in vivo*.

References

- [1] Guo-qiang Bi and Mu-ming Poo. *Synaptic modifications in cultured hippocampal neurons: dependence on spike timing, synaptic strength, and postsynaptic cell type*. Journal of Neuroscience, 1998.
- [2] György Buzsáki and Andreas Draguhn. *Neuronal oscillations in cortical networks*. Science, 2004.
- [3] Natalia Caporale and Yang Dan. Spike timing-dependent plasticity: a hebbian learning rule. 2008.
- [4] G. Bard Ermentrout and David H. Terman. *Mathematical Foundations of Neuroscience*. Springer, 2010.
- [5] MH Munk and S Neuenschwander. *High-frequency oscillations (20 to 120 Hz) and their role in visual processing*. Journal of Neurophysiology, 2000.
- [6] A Pogosyan, F Yoshida, CC Chen, I Martinez-Torres, T Foltyne, P Limousin, L Zrinzo, MI Hariz, and P Brown. *Parkinsonian impairment correlates with spatially extensive subthalamic oscillatory synchronization*. Neuroscience, 2010.

A Code Availability

All code used for simulations and analysis in this project is available at: <https://github.com/davidkelly2002/Mathematical-Biology-Project>. The repository includes implementations of the neural network model, spike-timing dependent plasticity, phase reductions, and scripts for generating the figures presented throughout this report.

B Detailed Neural Model Equations

The full dynamics for the ionic currents used in the Rubin–Terman thalamic neuron model are given below:

$$\begin{aligned} I_L(V) &= g_L(V - E_L), \\ I_{Na}(V, h) &= g_{Na}(m_\infty^3)h(V - E_{Na}), \\ I_K(V, h) &= g_K((0.75(1 - h))^4)(V - E_K), \\ I_T(V, r) &= g_T(p_\infty^2)r(V - E_T). \end{aligned}$$

The following steady-state functions and time constants are used for the gating variables:

$$\begin{aligned} h_\infty &= \frac{1}{1 + \exp\left(\frac{V+41}{4}\right)}, & r_\infty &= \frac{1}{1 + \exp\left(\frac{V+84}{4}\right)}, \\ \alpha_h &= 0.128 \exp\left(-\frac{V+46}{18}\right), & \beta_h &= \frac{4}{1 + \exp\left(-\frac{V+23}{5}\right)}, \\ \tau_h &= \frac{1}{\alpha_h + \beta_h}, & \tau_r &= 28 + \exp\left(-\frac{V+25}{10.5}\right), \\ m_\infty &= \frac{1}{1 + \exp\left(-\frac{V+37}{7}\right)}, & p_\infty &= \frac{1}{1 + \exp\left(-\frac{V+60}{6.2}\right)}. \end{aligned}$$

These expressions define the full conductance-based dynamics used in simulations and analysis throughout this study.